Spectral data analysis methods for the two-dimensional imaging diagnostics

Minjun J. Choi

National Fusion Research Institute, Daejeon 34133, Korea, Republic of

July 25, 2019

arXiv:1907.09184v2 [physics.data-an] 24 Jul 2019

Abstract

Some spectral data analysis methods that are useful for the two-dimensional imaging diagnostics data are introduced. It is shown that the frequency spectrum, the local dispersion relation, the flow shear, and the nonlinear energy transfer rates can be estimated using the proper analysis methods.

1 Introduction

Various two-dimensional imaging diagnostics have been developed to study the complicated dynamics of the tokamak fusion plasma. For example, the electron cyclotron emission imaging (ECEI) diagnostics, microwave imaging reflectometry (MIR), beam emission spectroscopy (BES) are utilized to measure the local electron temperature or density fluctuation and provide a more comprehensible picture.

Most advantages of the imaging diagnostics come from the inherent high-resolution multi-channel characteristics. Its strengths would be fully exploited when a proper data analysis method is used. There are already well developed spectral analysis methods in the literature. In this paper, we introduce some spectral analysis methods which are appropriate to the imaging diagnostics data. Some practical application examples using the ECEI data are also provided. It is shown that the frequency spectrum, the local dispersion relation (wavenumber-frequency spectrum), the flow shear, and the nonlinear energy transfer rates can be more accurately estimated using the proper analysis methods on the two-dimensional imaging data. In Appendix, the Python code package developed for the spectral and statistical analysis of the KSTAR diagnostics data is introduced briefly.

2 Spectral analysis methods for the imaging diagnostics

2.1 Frequency spectrum and the coherence estimation

The frequency spectrum of a discrete time series data is often estimated by the Fourier transform [1]. Let $X(f_p)$ be the discrete Fourier transform (DFT) of a discrete time series data $x(t_j)$. For each frequency index p, the DFT coefficient $X(f_p) = X_p$ is a complex value and it can be written as $X_p = A_p e^{i\alpha_p}$ where A_p represents a sinusoidal amplitude of the f_p frequency component in the time series data and α_p is its initial phase.

If an ideal fluctuation with the wavenumber $\mathbf{k}$ and the amplitude G is measured as an oscillation with the frequency $f = f_m$ by some diagnostics, we may expect to get $A_m \approx G$ from the DFT of the recorded signal. However, there is always noise component in the measured signal. The DFT coefficient at $f_p = f_m$, i.e. $X_m = A_m e^{i\alpha_m}$, will include the ideal fluctuation part ($G_x e^{i\delta_x}$) and the noise part ($N_x e^{in_x}$) where G_x and N_x are the measured fluctuation and noise amplitudes of the frequency f_m in $x(t_j)$, and δ_x and n_x are their initial phases, respectively (figure 1).

To reduce the noise contribution in the frequency spectrum estimation, we can utilize another measurement $y(t_j)$ by an adjacent channel separated by $\mathbf{d}$ and $|\mathbf{d}| < \lambda_c$ where λ_c is the correlation length of the fluctuation. Let $Y(f_p)$ be the DFT of $y(t_j)$. For the given frequency $f_p = f_m$, $Y_m = B_m e^{i\beta_m}$ will be composed of $G_y e^{i\delta_y}$ and $N_y e^{in_y}$ where G_y and N_y are the measured fluctuation and noise amplitudes of the frequency f_m in $y(t_j)$, and δ_y and n_y are their initial phases, respectively. Then, it is well known that the cross power spectrum can be obtained by the ensemble average of the N independent measurements of XY^* to reduce the noise part as follows.

$$P_{xy} = \langle XY^* \rangle = \frac{X^{(1)}Y^{(1)*} + ... + X^{(N)}Y^{(N)*}}{N} \tag{1}$$

where the superscripts indicate the measurement number. For the given frequency f_m, the 1st measurement can

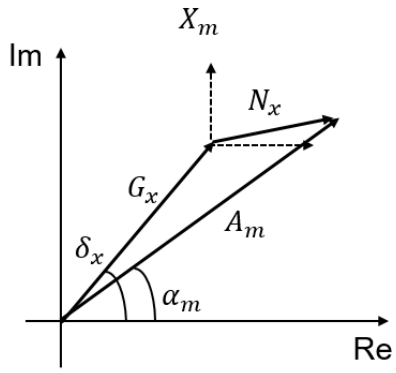

Figure 1: Representation of the Fourier transform coefficient in the complex plane

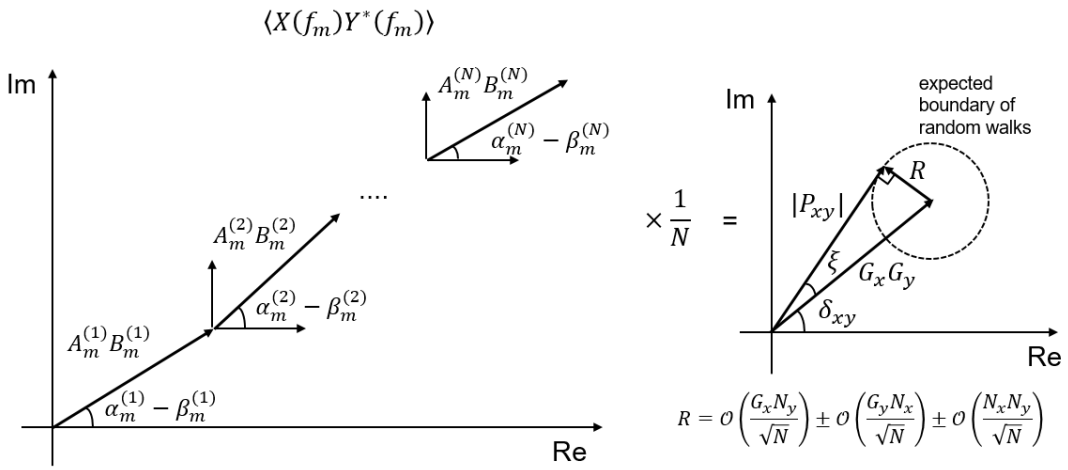

Figure 2: Ensemble average in the complex plane

be written as follows.

$$\begin{aligned} X_m^{(1)}Y_m^{(1)*} &= A_m^{(1)}e^{i\alpha_m^{(1)}}(B_m^{(1)}e^{i\beta_m^{(1)}})^* \\ &= (G_x^{(1)}e^{i\delta_x^{(1)}} + N_x^{(1)}e^{in_x^{(1)}})(G_y^{(1)}e^{-i\delta_y^{(1)}} + N_y^{(1)}e^{-in_y^{(1)}}) \\ &= G_x^{(1)}G_y^{(1)}e^{i(\delta_x^{(1)}-\delta_y^{(1)})} + G_x^{(1)}N_y^{(1)}e^{i(\delta_x^{(1)}-n_y^{(1)})} + N_x^{(1)}G_y^{(1)}e^{i(n_x^{(1)}-\delta_y^{(1)})} + N_x^{(1)}N_y^{(1)}e^{i(n_x^{(1)}-n_y^{(1)})} \end{aligned} \quad (2)$$

In the above equation, each term can be thought as a vector in the complex plane. If we choose the separation time between the measurements longer than the correlation time of the noise, the initial phases of the noise (n_x and n_y) and all $\delta_x - n_y$, $n_x - \delta_y$, and $n_x - n_y$ will be random in each measurement. Adding up vectors in the complex plane with the random phase will be like a random walk (RW) diffusion whose expected deviation is (step size) $\times \sqrt{N}$. The division by N in the ensemble average will make the random phase terms decay with $1/\sqrt{N}$. On the other hand, the first term has the non-random definite phase, $\delta_x^{(1)} - \delta_y^{(1)}$, which is the ideal fluctuation phase difference between two channels, i.e. $\delta_x^{(1)} - \delta_y^{(1)} \equiv \delta_{xy} = \mathbf{k} \cdot \mathbf{d}$. The ensemble average in the cross power calculation will lead to

$$\langle X_m Y_m^* \rangle = G_x G_y e^{-i\delta_{xy}} + \frac{\mathrm{RW}(G_xN_y) + \mathrm{RW}(G_yN_x) + \mathrm{RW}(N_xN_y)}{N} \quad (3)$$

where $\mathrm{RW}(C)$ represents the random walk with the amplitude C in the complex plane (figure 2). The amplitude of the cross power can be written as

$$|\langle X_m Y_m^* \rangle| = G_x G_y \pm \mathcal{O}\left(\frac{G_xN_y}{\sqrt{N}}\right) \pm \mathcal{O}\left(\frac{G_yN_x}{\sqrt{N}}\right) \pm \mathcal{O}\left(\frac{N_xN_y}{\sqrt{N}}\right) \quad (4)$$

Therefore, the cross power provides a significant noise reduction in the spectrum estimation for the large N. The imaging diagnostics with many channels is favorable to find a proper pair of channels to calculate the cross power for a specific mode or event.

Note that it is convenient to normalize the cross power spectrum with the auto power spectra as follows.

$$\gamma_{xy} = \frac{|\langle XY^* \rangle|}{\sqrt{\langle XX^* \rangle}\sqrt{\langle YY^* \rangle}} \quad (5)$$

It is called the coherence and ranges from 0 to 1. It means the coherent ($\mathbf{k}\cdot\mathbf{d} \approx$ const) fluctuation power fraction against the total power. The noise floor in the coherence will be given as $\frac{|\langle N_x N_y e^{-i(n_x - n_y)}\rangle|}{N_x N_y} \approx 1/\sqrt{N}$.

2.2 Local wavenumber and the flow shear estimation

The phase difference between the measured signal $x(t_j)$ and $y(t_j)$ is another important quantity. This cross phase can be obtained as

$$\theta_{xy} = \tan^{-1}\left[\frac{\mathrm{Im}[P_{xy}]}{\mathrm{Re}[P_{xy}]}\right] \tag{6}$$

where P_{xy} is the cross power. From figure 2, we can see that $\theta_{xy} = \delta_{xy} \pm \mathcal{O}(\xi)$ where δ_{xy} is the phase difference by the mode $\mathbf{k}$ between two channels, i.e. $\delta_{xy} = \mathbf{k}\cdot\mathbf{d}$, and ξ is the noise contribution. The maximum possible noise contribution is

$$\xi = \sin^{-1}\left[\frac{R}{G_x G_y}\right] \approx \frac{2\epsilon}{\sqrt{N}} + \frac{\epsilon^2}{\sqrt{N}} + \mathcal{O}\left(\frac{\epsilon^3}{N^{3/2}}\right) + ... \tag{7}$$

with the small parameter expansion $\epsilon = |N_x/G_x| \approx |N_y/G_y| < 1$. For the large N or the large signal-to-noise ratio $1/\epsilon \gg 1$, $\theta_{xy} \approx \delta_{xy} = \mathbf{k}\cdot\mathbf{d}$, which means that we can estimate the wavenumber in the direction of $\mathbf{d}$ using the cross phase. In other words, the cross phase $\theta_{xy}(f)$ can be interpreted as the estimation of the local dispersion relation $K(\omega) = \delta_{xy}(\omega)/d \approx \theta_{xy}(\omega)/d$ where K is the local wavenumber along the $\mathbf{d}$ direction and $\omega = 2\pi f$ is the measured angular frequency. The local poloidal or radial dispersion relation can be obtained with the imaging diagnostics by using the channels separated in the poloidal or radial direction within the correlation length, respectively.

Using the local dispersion relation, the phase velocity (ω/K) or the group velocity ($\partial\omega/\partial K$) of the fluctuation in the laboratory frame can be obtained. The laboratory frame phase or group velocity v_L measurement is composed of v_d and v_p where v_d is the plasma flow and the v_p is the phase or group velocity in the plasma frame. If we can assume that the v_p is nearly uniform in the measurement area, the spatial gradient of the v_L corresponds to the spatial gradient of the plasma flow, i.e. $\nabla v_L \approx \nabla v_d$, which is often more important in tokamak plasmas.

2.3 Local wavenumber-frequency spectrum estimation

Following the method introduced in [2], the local wavenumber-frequency spectrum $S_L(K, f)$ can be estimated as

$$S_L(K, f) = \left\langle \left(\frac{X(f)X^*(f) + Y(f)Y^*(f)}{2}\right) \delta_D\left[\frac{\delta_{xy}(f)}{d} - K\right]\right\rangle \tag{8}$$

where $\delta_D[\cdot]$ represents the Dirac delta function and δ_{xy} can be estimated by the cross phase calculated from each measurement. This provides how the fluctuation power is distributed in the wavenumber K and frequency f space by means of a histogram [2]. $S_L(K, f)$ can be more informative than the local dispersion relation, but it is not easy to identify the noise contribution. The imaging diagnostics could allow a more accurate estimation as used in [3], since multi-pairs of the channels along the same direction can be utilized to perform the ensemble average $\langle S_L(K, f)\rangle_p$ where $\langle\cdot\rangle_p$ represents the average over pairs.

2.4 Bispectrum and bicoherence estimation

The nonlinear wave-wave coupling can be identified based on the fact that the coupled waves would have a well-defined phase relation [4]. Consider three waves with the amplitudes G_1, G_2, and G_3 and frequencies f_1, f_2, and $f_3 = f_1 + f_2$ (satisfying the frequency resonance condition [4]), measured in $x(t_j)$ by a single channel. The (auto) bispectrum is defined as below to investigate the phase coupling among the waves.

$$B(f_1, f_2) = \langle X_1 X_2 X_3^*\rangle \tag{9}$$

The 1st measurement will be

$$X_1^{(1)} X_2^{(1)} X_3^{(1)*} = G_1^{(1)} G_2^{(1)} G_3^{(1)} e^{i(\delta_1^{(1)} + \delta_2^{(1)} - \delta_3^{(1)})} + ... \tag{10}$$

where δ_1, δ_2, and δ_3 represent the initial phase of each wave f_1, f_2, and f_3, respectively. If the three waves are excited independently, their phases will not be related. Then, $\delta_1 + \delta_2 - \delta_3$ will be random in each measurement and the $G_1 G_2 G_3$ term will decay with $1/\sqrt{N}$ in the ensemble average. On the other hand, if they are nonlinearly coupled, $\delta_1 + \delta_2 - \delta_3 =$ const and the $G_1 G_2 G_3$ term will remain as the most significant term. The bispectrum with f_1, f_2 and $f_3 = f_1 + f_2$ is known to be useful to measure the statistical dependence between three waves.

In practice, the squared bicoherence (the normalized squared bispectrum) is often used to measure the degree of the nonlinear coupling, because we have the finite N measurements and the $1/\sqrt{N}$ decay may not be sufficient for the large amplitudes. The squared bicoherence is defined as follows.

$$b^2(f_1, f_2) = \frac{|\langle X_1 X_2 X_3^*\rangle|^2}{\langle |X_1 X_2|^2\rangle\langle |X_3|^2\rangle} \tag{11}$$

This value ranges from 0 to 1, meaning the fraction of the power at f_3 due to the coupling against the total power at f_3. $\langle |X_3|^2 \rangle$ represents the total power at f_3 and $\frac{|\langle X_1 X_2 X_3^* \rangle|^2}{\langle |X_1 X_2|^2 \rangle}$ is the power at f_3 due to the coupling with f_1 and f_2 [4].

Note that if we want to calculate the cross bispectrum using another channel (e.g. $\langle X_1 X_2 Y_3^* \rangle$), the channels should be selected carefully that $\mathbf{d} \cdot \nabla v_d = 0$ since the different flow velocities would break the frequency resonance condition in the measurements. The auto bispectrum might be more preferred unless we have a particular reason as described below.

2.5 Nonlinear energy transfer estimation

It was shown that the bispectrum or the (squared) bicoherence can measure the degree of the nonlinear coupling. For the simplest system in which the third wave (f_3) is just the result of a single three-wave coupling with the others, i.e. $G_3 = Q^3_{1,2} G_1 G_2$, the coupling coefficient can be estimated as $Q^3_{1,2} \approx \frac{B^*(f_1,f_2)}{\langle |X_1 X_2|^2 \rangle}$ for the large signal-to-noise ratio [4]. However, the real system is more complicated and a mode evolves through more than one nonlinear coupling.

For some physical quantity $\phi(z,t)$ at position z and time t, we can decompose $\phi(z,t)$ with the wavenumber Fourier coefficients such as $\phi(z,t) = \sum_p \Phi(k_p,t) e^{ik_p z}$ and study its temporal evolution for each k_p, or decompose it with the frequency Fourier coefficients such as $\phi(z,t) = \sum_p \Phi(z,\omega_p) e^{i\omega_p t}$ and study its spatial evolution for each ω_p. The former requires at least two-point temporal measurements of the wavenumber spectrum [5], and the later requires two-point spatial measurements of the frequency spectrum [6]. We can choose the frequency decomposition and consider the following evolution equation [6].

$$\frac{\partial \Phi(z,\omega_p)}{\partial z} = \Lambda^L_{\omega_p} \Phi(z,\omega_p) + \sum_{\substack{p_1 \geq p_2 \\ p = p_1 + p_2}} \Lambda^Q_{\omega_{p_1},\omega_{p_2}} \Phi(z,\omega_{p_1}) \Phi(z,\omega_{p_2}) + ... \tag{12}$$

where $\Lambda^L_{\omega_p}$ and $\Lambda^Q_{\omega_{p_1},\omega_{p_2}}$ are the linear and quadratic coupling coefficients, respectively. To use the two-point measurements at z and $z+d$, we need to discretize the above equation to reconstruct the following system [7].

$$Y_p = L_p X_p + \sum_{\substack{p_1 \geq p_2 \\ p = p_1 + p_2}} Q^p_{p_1,p_2} X_{p_1} X_{p_2} + ... \tag{13}$$

where X_p and Y_p represent the measured Fourier coefficients at the position z and $z+d$, respectively, L_p is the linear transfer function, and $Q^p_{p_1,p_2}$ is the quadratic transfer function. It is to estimate those transfer functions which transform X_p into Y_p. The linear and quadratic transfer functions for such a system can be calculated with the Millionshchikov hypothesis ($\langle X_{p_1} X_{p_2} X^*_{p_3} X^*_{p_4} \rangle \approx \langle |X_{p_1} X_{p_2}|^2 \rangle$) as shown in [7, 8].

$$L_p = \frac{\langle Y_p X^*_p \rangle - \sum_{\substack{p_1 \geq p_2 \\ p = p_1 + p_2}} \frac{\langle X_{p_1} X_{p_2} X^*_p \rangle \langle X^*_{p_1} X^*_{p_2} Y_p \rangle}{\langle |X_{p_1} X_{p_2}|^2 \rangle}}{\langle X_p X^*_p \rangle - \sum_{\substack{p_1 \geq p_2 \\ p = p_1 + p_2}} \frac{|\langle X_{p_1} X_{p_2} X^*_p \rangle|^2}{\langle |X_{p_1} X_{p_2}|^2 \rangle}} \tag{14}$$

$$Q^p_{p_1,p_2} = \frac{\langle X^*_{p_1} X^*_{p_2} Y_p \rangle - L_p \langle X^*_{p_1} X^*_{p_2} X_p \rangle}{\langle |X_{p_1} X_{p_2}|^2 \rangle} \tag{15}$$

Or, we can directly solve the following matrix equation for $\mathbf{H}$ with the large number of ensembles ($N \gg$ the number of unknowns in $\mathbf{H}$) [6].

$$\mathbf{Y} = \mathbf{X}\mathbf{H} \tag{16}$$

where

$$\mathbf{Y} = \begin{bmatrix} Y^{(1)}_p \\ Y^{(2)}_p \\ \vdots \\ Y^{(N)}_p \end{bmatrix} \quad \mathbf{X} = \begin{bmatrix} X^{(1)}_p & X^{(1)}_{p_1} X^{(1)}_{p-p_1} & X^{(1)}_{p_2} X^{(1)}_{p-p_2} & ... \\ X^{(2)}_p & X^{(2)}_{p_1} X^{(2)}_{p-p_1} & X^{(2)}_{p_2} X^{(2)}_{p-p_2} & ... \\ \vdots & \vdots & \vdots & ... \\ X^{(N)}_p & X^{(N)}_{p_1} X^{(N)}_{p-p_1} & X^{(N)}_{p_2} X^{(N)}_{p-p_2} & ... \end{bmatrix} \quad \mathbf{H} = \begin{bmatrix} L_p \\ Q^p_{p_1,p-p_1} \\ Q^p_{p_2,p-p_2} \\ \vdots \end{bmatrix} \tag{17}$$

Verification results of the Ritz [7, 8] and Wit [6] methods using the model L_p and $Q^p_{p_1,p_2}$ are shown in figure 3. The following model equations are used for L_p and $Q^p_{p_1,p_2}$ to generate Y_p from X_p [7].

$$L_p = 1.0 - 0.4 \frac{p}{p^2_{Nyq}} + i0.8 \frac{p}{p_{Nyq}} \tag{18}$$

$$Q^p_{p_1,p_2} = \frac{i}{5p^4_{Nyq}} \frac{p_1 p_2 (p_2^2 - p_1^2)}{1 + p^2/p^2_{Nyq}} \tag{19}$$

where p_{Nyq} is the index of the Nyquist frequency (250 kHz in this case). For X_p, the non-Gaussian (skewness$\sim$ 3 and kurtosis$\sim$ 7) time series data from the ECEI diagnostics was used.

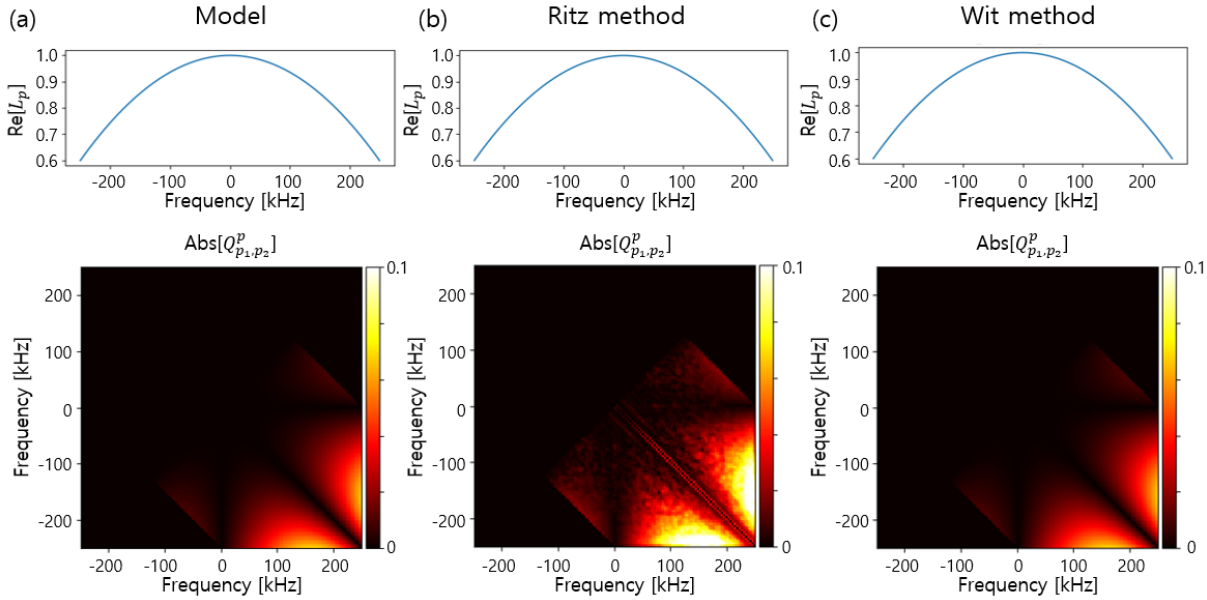

Figure 3: (Color online) (a) The real part of L_p and $|Q^p_{p_1,p_2}|$ from the model equation. Estimation results using (b) the Ritz and (c) Wit method.

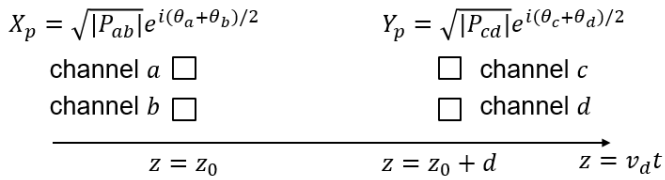

Figure 4: Reconstruction of X_p and Y_p using multiple channels of the imaging diagnostics. With the Taylor hypothesis, the spectra can be obtained from the single pair measurements separated by δt instead of the measurements of two pairs separated by d.

It was reporeted that the Ritz method can suffer from the artificial damping or amplifying via the auto power in the denominator of L_p [7, 8]. Since the imaging diagnostics have multiple channels, we may reconstruct the noise-reduced X_p and Y_p using the local cross power spectrum at z and $z+d$, respectively. For example, we can obtain the cross power $P_{ab} = \langle X_{(a)} X^*_{(b)} \rangle$ using two channels (a and b) near $z = z_0$ and take the amplitude of the cross power as $A_p = \sqrt{|P_{ab}(f_p)|}$, and take their average phases as α_p where $X_p = A_p e^{i\alpha_p}$. We can utilize another pair of c and d near $z = z_0 + d$ to reconstruct $Y_p = \sqrt{|P_{cd}(f_p)|}e^{i\beta_p}$ (figure 4).

Once the transfer functions (L_p and $Q^p_{p_1,p_2}$) are estimated from X_p and Y_p either using the Ritz or Wit method, we can calculate the linear growth rate γ_p and the nonlinear energy transfer rate T_p for the spectral power $P_p = \langle X_p X_p^* \rangle$ whose evolution is described as

$$\frac{\partial P_p}{\partial t} \approx \frac{\langle Y_p Y_p^* \rangle - \langle X_p X_p^* \rangle}{\delta t} = \gamma_k P_k + T_k \tag{20}$$

where [8]

$$\gamma_p \approx \frac{|L_p|^2 - 1}{\delta t} \tag{21}$$

$$T_p \approx 2\,\mathrm{Re}\left[L_p^* \sum_{\substack{p_1 \geq p_2 \\ p = p_1 + p_2}} \frac{Q^p_{p1,p2} \langle X_{p1} X_{p2} X_p^* \rangle}{\delta t} \right] + \sum_{\substack{p_1 \geq p_2 \\ p = p_1 + p_2}} \sum_{\substack{p_3 \geq p_4 \\ p = p_3 + p_4}} \frac{Q^p_{p1,p2} Q^{p*}_{p3,p4} \langle X_{p1} X_{p2} X^*_{p3} X^*_{p4} \rangle}{\delta t} \tag{22}$$

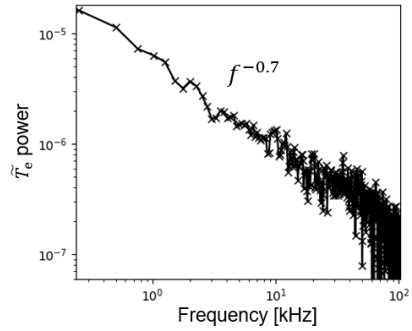

Figure 5: The power spectrum of the event size exhibits the power-law behavior.

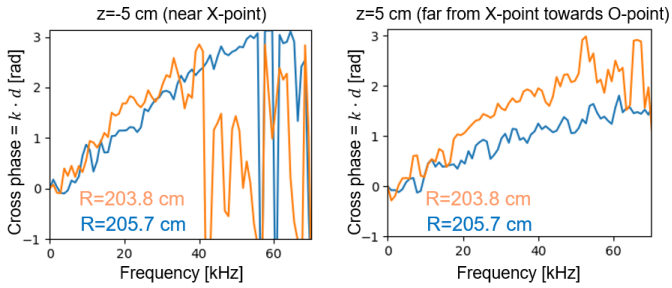

Figure 6: The cross phase measurements in different regions outside the magnetic island.

3 Application of the spectral analysis methods to the electron cyclotron emission imaging diagnostics data

3.1 Frequency spectrum measurement

An accurate measurement of the frequency spectrum is not only the basis of all spectral analyses but it is an important element to validate the transport model. The non-diffusive transport model based on the self-organized criticality predicts the power-law behavior of the avalanche event size power spectrum $S(f) \propto f^{-\alpha}$ where $\alpha = 1$ for the ideal case and $0 < \alpha < 1$ for the case including a subdominant diffusive transport [9, 10]. In the KSTAR plasma where the avalanche-like events are observed, two ECEI channels on the same flux surface are used to estimate the event size (δT_e) power spectrum via the cross power. Figure 5 shows the power spectrum of the normalized event size $\tilde{T}_e = \delta T_e / \langle T_e \rangle$ which exhibits the power-law behavior $S(f) \propto f^{-0.7}$. The accurate power spectrum measurement corroborates the non-diffusive avalanche-like characteristics of the observed transport event [11].

3.2 Flow shear measurement

The radial shear of the flow is important since it can suppress the mode whose growth rate is smaller than the flow shear. As discussed in Section 2.2, the flow shear can be estimated using the cross phase measurements between two channels. Figure 6 shows the cross phase $\delta_{xy}(f) = k(f)d$ measurements using channel pairs in different regions outside the magnetic island boundary. Since the local group velocity of the fluctuations is inversely proportional to the slope of the $\delta_{xy}(f)$ measurement, the local group velocity and its radial shear are both stronger in the region far from X-point. Considering that the toroidal flow is negligible and the intrinsic group velocity of the fluctuations is nearly constant in the measurement area, the observed radial shear of the local group velocity is attributed to the poloidal $E \times B$ flow shear [12]. This finding explained that the fluctuation power becomes weaker as it goes far from X-point [12, 13, 14].

3.3 Nonlinear interaction measurement (preliminary)

Identifying the nonlinear interaction between multiple modes is important to understand the nonlinear growth and damping of the modes. In some experiments of the edge localized mode (ELM) suppression by the resonant magnetic perturbation field, the amplitude of the broadband fluctuations increases as the ELM fluctuation amplitude decreases [3]. The nonlinear energy transfer from the ELM to the broadband fluctuations was suggested as a key mechanism for the ELM crash suppression. The bispectral analysis could identify the existence of the nonlinear interaction between the ELM ($f \sim 20$ kHz) and the broadband fluctuations ($0 \leq f \leq 100$ kHz) [3]. In addition, figure 7 shows the estimation of the linear growth rate and nonlinear energy transfer rate for the ELM crash suppression phase using equations (21) and (22) and the Wit method in Section 2.5. A single pair of ECEI channels at the pedestal are used to obtain both X_p and Y_p with the Taylor hypothesis. The estimation results

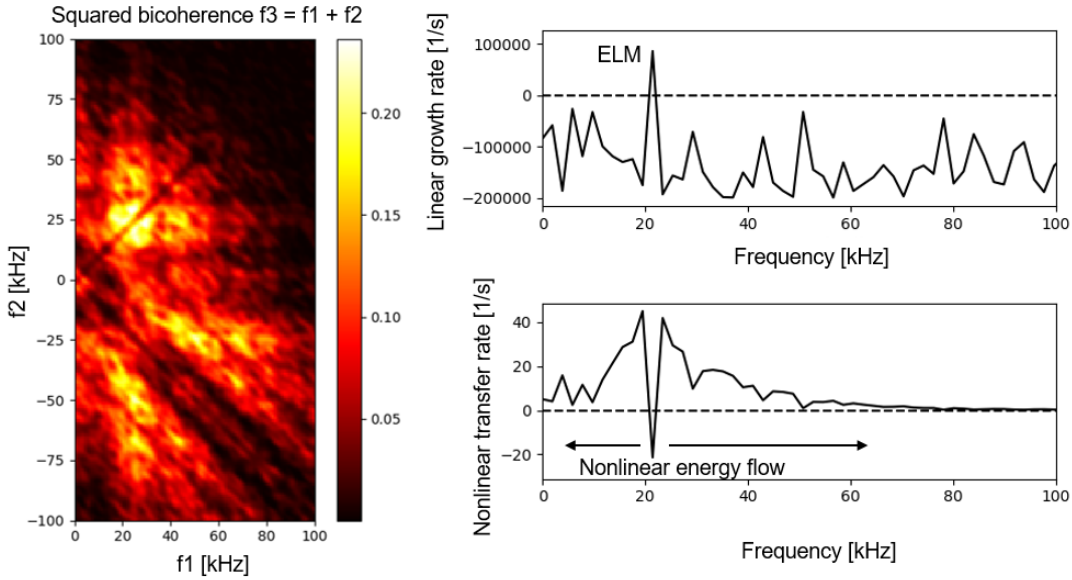

Figure 7: Spectral analysis of the nonlinear interaction during the ELM crash suppression phase.

suggest that the ELM is linearly unstable and its energy is transferred broadly to the other modes via nonlinear coupling, which may explain the ELM crash suppression. Nevertheless, it should be noted that the estimation of the rates is not very robust probably due to the noise contributions, and more verification of this analysis would be necessary.

4 Summary

The spectral methods which are more beneficial with the imaging diagnostics are introduced. In addition, the strengths of the imaging diagnostics in investigating the frequency spectrum, the local dispersion relation, the flow shear, and the nonlinear interaction have been demonstrated with practical applications.

5 Appendix

5.1 fluctana

The Python code package named as "fluctana" has been developed to provide an easy access and analysis of the various fluctuation data of the KSTAR tokamak. It includes all the spectral methods introduced in this paper as well as the statistical methods to calculate the higher order moments, the Hurst exponent, the Jensen-Shannon complexity and the normalized Shannon entropy, and the transfer entropy. The code and simple tutorials are available via the GitHub repository `https://github.com/minjunJchoi/fluctana`.

References

[1] P. D. Welch, "The Use of Fast Fourier Transform for the Estimation of Power Spectra: A Method based on Time Averaging Over Short, Modified Periodograms," *IEEE Transactions on audio and electroacoustics*, vol. AU-15, pp. 70–73, Feb. 1967.

[2] J. M. Beall, Y. C. Kim, and E. J. Powers, "Estimation of wavenumber and frequency spectra using fixed probe pairs," *Journal of Applied Physics*, vol. 53, pp. 3933–3940, June 1998.

[3] J. Lee, G. S. Yun, M. J. Choi, J.-M. Kwon, Y.-M. Jeon, W. Lee, N. C. Luhmann, and H. K. Park, "Nonlinear Interaction of Edge-Localized Modes and Turbulent Eddies in Toroidal Plasma undern=1Magnetic Perturbation," *Physical Review Letters*, vol. 117, no. 7, p. 075001, 2016.

[4] Y. C. Kim and E. J. Powers, "Digital Bispectral Analysis and Its Applications to Nonlinear Wave Interactions," *IEEE Transactions on Plasma Science*, vol. PS-7, no. 2, pp. 120–131, 1979.

[5] C. P. Ritz, E. J. Powers, and R. D. Bengtson, "Experimental measurement of three-wave coupling and energy cascading," *Physics of Fluids B: Plasma Physics*, vol. 1, pp. 153–163, Jan. 1989.

[6] T. D. Wit, V. V. Krasnosel'Skikh, M. Dunlop, and H. Lühr, "Identifying nonlinear wave interactions in plasmas using two-point measurements: A case study of Short Large Amplitude Magnetic Structures (SLAMS)," *Journal of Geophysical Research: Atmospheres*, vol. 104, pp. 17079–17090, Aug. 1999.

[7] C. P. Ritz and E. J. Powers, "Estimation of nonlinear transfer functions for fully developed turbulence," *Physica D: Nonlinear Phenomena*, vol. 20, pp. 320–334, June 1986.

[8] J. S. Kim, R. D. Durst, R. J. Fonck, E. Fernandez, a. Ware, and P. W. Terry, "Technique for the experimental estimation of nonlinear energy transfer in fully developed turbulence," *Physics of Plasmas*, vol. 3, no. 11, pp. 3998–3998, 1996.

[9] R. Sanchez and D. E. Newman, "Self-organized criticality and the dynamics of near-marginal turbulent transport in magnetically confined fusion plasmas," *Plasma Physics and Controlled Fusion*, vol. 57, no. 12, p. 123002, 2015.

[10] T. S. Hahm and P. H. Diamond, "Mesoscopic Transport Events and the Breakdown of Fick's Law for Turbulent Fluxes ," *Journal of the Korean Physical Society*, vol. 73, pp. 747–792, July 2018.

[11] M. J. Choi, H. Jhang, J.-M. Kwon, J. Chung, M. Woo, L. Qi, S. Ko, T.-S. Hahm, H. K. Park, H.-S. Kim, J. Kang, J. Lee, M. Kim, and G. S. Y. and, "Experimental observation of the non-diffusive avalanche-like electron heat transport events and their dynamical interaction with the shear flow structure," *Nuclear Fusion*, vol. 59, p. 086027, June 2019.

[12] M. J. Choi, J. Kim, J. M. Kwon, H. K. Park, Y. In, W. Lee, K. D. Lee, G. S. Yun, J. Lee, M. Kim, W. H. Ko, J. H. Lee, Y. S. Park, Y. S. Na, N. C. Luhmann Jr, and B. H. Park, "Multiscale interaction between a large scale magnetic island and small scale turbulence," *Nuclear Fusion*, vol. 57, p. 126058, Dec. 2017.

[13] J.-M. Kwon, S. Ku, M. J. Choi, C. S. Chang, R. Hager, E. S. Yoon, H. H. Lee, and H. S. Kim, "Gyrokinetic simulation study of magnetic island effects on neoclassical physics and micro-instabilities in a realistic KSTAR plasma," *Physics of Plasmas*, vol. 25, p. 052506, May 2018.

[14] K. S. Fang and Z. Lin, "Global gyrokinetic simulation of microturbulence with kinetic electrons in the presence of magnetic island in tokamak," *Physics of Plasmas*, vol. 26, p. 052510, May 2019.